Effects of Defects on Band Structure and Excitons in WS_2 Revealed by Nanoscale Photoemission Spectroscopy

Christoph Kastl[1], Roland J. Koch[1,2], Christopher T. Chen[1], Johanna Eichhorn[3], Søren Ulstrup[2,4], Aaron Bostwick[2], Chris Jozwiak[2], Tevye R. Kuykendall[1], Nicholas J. Borys[5], Francesca M. Toma[3], Shaul Aloni[1], Alexander Weber-Bargioni[1], Eli Rotenberg[2], Adam M. Schwartzberg[1*]*

[1]The Molecular Foundry, Lawrence Berkeley National Laboratory, Berkeley, California 94720, USA

[2]Advanced Light Source, Lawrence Berkeley National Laboratory, Berkeley, California 94720, USA

[3]Chemical Sciences Division, Lawrence Berkeley National Laboratory, Berkeley, California 94720, USA

[4]Department of Physics and Astronomy, Interdisciplinary Nanoscience Center (iNANO), Aarhus University, 8000 Aarhus C, Denmark

[5]Department of Physics, Montana State University, Bozeman, Montana 59717, USA.

*E-mail: ckastl@lbl.gov

*E-mail: amschwartzberg@lbl.gov

KEYWORDS. transition metal dichalcogenides, defects, photoemission spectroscopy, chemical vapor deposition, excitons.

ABSTRACT.

Two-dimensional materials with engineered composition and structure will provide designer materials beyond conventional semiconductors. However, the potentials of defect engineering remain largely untapped, because it hinges on a precise understanding of electronic structure and excitonic properties, which are not yet predictable by theory alone. Here, we utilize correlative, nanoscale photoemission spectroscopy to visualize how local introduction of defects modifies electronic and excitonic properties of two-dimensional materials at the nanoscale. As a model system, we study chemical vapor deposition grown monolayer WS_2, a prototypical, direct gap, two-dimensional semiconductor. By cross-correlating nanoscale angle resolved photoemission spectroscopy, core level spectroscopy and photoluminescence, we unravel how local variations in defect density influence electronic structure, lateral band alignment and excitonic phenomena in synthetic WS_2 monolayers.

Transition metal dichalcogenides (TMDs) and other layered materials have recently regained significant interest because of their emergent properties when reduced to single layers.[1,2] Atomically thin layers of TMDs provide a versatile and structurally commensurate library of two-dimensional (2D) materials, with the most prominent examples being the tungsten and molybdenum-based semiconductors MoS_2, $MoSe_2$, WS_2 and WSe_2. These materials form a toolbox for studying fundamental quantum phenomena in low-dimensional solid state systems as

well as for future applications in electronics, optics or catalysis.[3–5] Due to the strong electronic confinement and the reduced electrostatic screening in two dimensions,[2,6] the electronic and optical properties of 2D materials are generally more susceptible to strain, surface modifications or structural defects than those of their bulk counterparts.[7–9] While structural defects in semiconductors are usually considered detrimental, the large tunability of 2D materials provides an effective way to create functional properties by defect engineering beyond the conventional concept of doping in bulk semiconductors.[10] For example, point defects in TMDs are considered to enable single photon quantum emitters and to represent active sites in catalytic processes on the otherwise inert TMD surfaces,[5,11,12] while line defects are predicted to act as spin polarizers and have been shown to host exotic quantum phases, such as charge density waves.[13,14] Although defect structures with similar functionality exist also in bulk materials, *e.g.* color centers in wide gap semiconductors, the interfacial nature of 2D materials provides enhanced opportunities to access, utilize and even combine different defect types in a controlled manner and to engineer functionality in these materials. However, such defect engineering necessitates a complete characterization and understanding how their electronic and optical properties are modified at the nanoscale. So far, structural defects in 2D TMDs have been studied experimentally either directly by atomic resolution scanning probe and electron microscopy or indirectly by diffraction limited optical methods.[8,15–19] Although scanning probe and electron microscopy provide unmatched spatial resolution, these methods often lack information about macroscopic parameters, such as chemical composition and ordering effects. Yet, a multimodal cross-correlative approach with information about structure-function-relationships is particularly useful for understanding properties of low-dimensional materials at the nanoscale. The interplay between phenomena at different relevant length scales, such as inter-defect distances, the exciton

Bohr radius, screening lengths, crystal domain sizes, and exciton diffusion lengths, gives rise to a complex nanoscale heterogeneity of the optical and electronic properties.[20,21] For example, recent experiments achieved an indirect correlation between the atomic structure measured at the sub-nano scale and the excitonic properties measured at the sub-micron scale.[19] Especially in view of integrating functional 2D materials into wafer-scale (opto)electronics, it will also be critical to understand the role of spatial inhomogeneity on electronic and optical functionality.

Here, we utilize correlative, nanoscale photoemission spectroscopy as a powerful tool to study electronic and chemical properties of 2D materials with a spatial resolution down to 150 nm. As a model system, we study chemical vapor deposition (CVD) grown monolayer WS_2, a prototypical direct gap semiconductor of the TMD family. By cross-correlating multimodal information from nanoscale angle resolved photoemission spectroscopy (nano-ARPES), nanoscale core level spectroscopy (nano-XPS) and micro-photoluminescence (μPL) imaging, we unravel how local variations in defect density influence electronic structure, lateral band alignment and excitonic phenomena in synthetic monolayer WS_2.

Results and discussion

Nano-ARPES necessitates a flat and conductive substrate that has a well-defined surface normal vector for preserving momentum resolution. While h-BN and epitaxial graphene can be excellent substrates for photoemission studies of 2D materials, where very narrow linewidths and a high degree of decoupling from the conductive support material are achieved,[22–24] supporting 2D materials on high-k oxides, such as TiO_2 or $SrTiO_3$, adds the possibility of tuning the electronic properties *via* the dielectric properties of the substrate.[25] First, the stoichiometry of the oxide substrates (*i.e.* oxygen concentration) can control the charge doping from the substrate to

the 2D materials. Second, complex metal oxides are known to host a range of correlated phenomena, and therefore the ability to interface 2D materials and strongly correlated materials provides significant opportunities for engineering emerging interface phenomena in these material systems.[26] In this context, Nb-doped rutile TiO_2 has been demonstrated to be suitable as substrate for photoemission studies of transferred 2D materials.[22] In the temperature range that is commonly used for growth of tungsten based TMDs (~800 °C - 900 °C), [27,28] the TiO_2 substrate is etched by reducing agents such as sulfur or hydrogen (Supporting Information S1). Therefore, we utilized a water-assisted, low-temperature CVD-process to directly grow monolayer WS_2 on TiO_2 single crystal substrates.[29] Pre-depositing a WO_3 layer onto the TiO_2 substrate by atomic layer deposition and using perylene-3,4,9,10-tetracarboxylic acid tetrapotassium salt (PTAS) as seeding promoter, we synthesized micro-domains of WS_2 at a growth temperature of 600 °C that exhibit mostly dendritic shapes and a surface coverage of approximately 50%, (Figure 1a). This growth temperature is among the lowest for WS_2 monolayers that has been reported in literature.

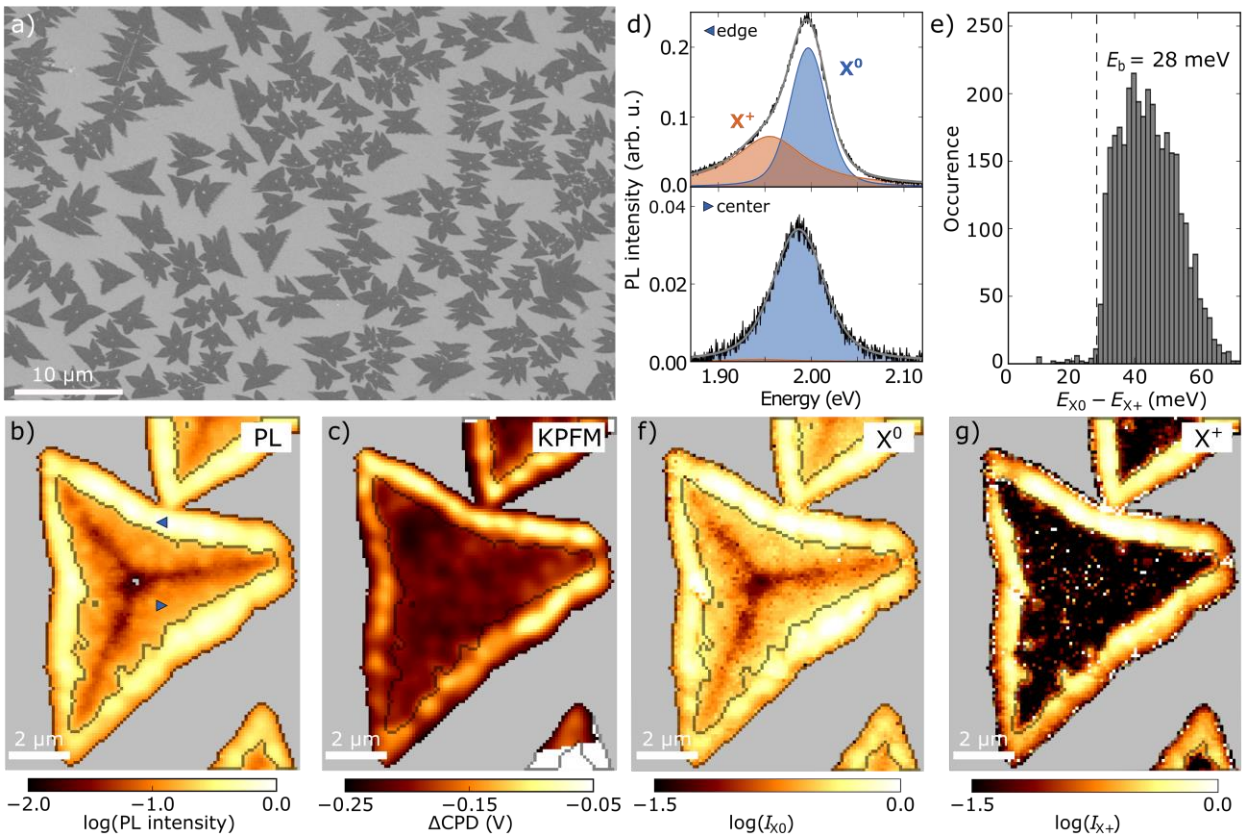

Figure 1. Correlating excitons, trions and surface potential in WS_2 monolayers. **(a)** Electron microscope image of CVD grown WS_2 (dark) on TiO_2 (light). **(b)** Integrated photoluminescence (PL) intensity of a WS_2 monolayer (log-scale) showing a bright edge region and a dim center region. For the sake of clarity, these regions are separated by a gray line. The gray areas indicate the substrate. **(c)** Contact potential difference map ($\Delta CPD = \phi_{sample} - \phi_{tip}$) of the same region as in **b** imaged with Kelvin probe force microscopy (KPFM). The CPD indicates an upwards shift of the bands in the edge region. **(d)** Representative PL spectra from the edge and from the center (triangles in (b)). At the edge, the spectrum is deconvolved into a main peak at E_{X0} = 2.0 eV (neutral exciton) and a low energy shoulder at E_{X+} = 1.96 eV (charged trion). At the center, the spectrum is well described by a single peak at E_{X0} = 1.98 eV. **(e)** Histogram of E_{X0} - E_{X+}. The

cut-off of the histogram at 28 meV (dashed line) coincides with the trion binding energy in WS_2. Spatial maps of **(f)** exciton emission intensity I_{X0} and **(g)** trion emission intensity I_{X+}.

Atomic force microscopy and Raman spectroscopy (Supporting Information S1) confirm that the domains consist exclusively of monolayers. Most of the micro domains exhibit point-like contaminations around the center (Figure 1a), which are likely nucleation sites.[30] Figure 1b displays a spatially resolved PL intensity map of a monolayer domain under ambient conditions. The overall PL efficiency is enhanced near the edges compared to the center region of the domain. Within the center region, lines of quenched PL are visible, which can be assigned to inter-grain boundaries.[31] Intensity and spectral variations of PL emission that are correlated with morphological features, such as grain boundaries and edge regions, are commonly observed in synthetic 2D materials, which is attributed to material heterogeneity caused by variations in the growth process.[20,29,32,33] Especially for large scale synthesis of functional 2D materials, it is important to understand the impact of such nanoscale heterogeneity on the electronic and optical properties. Therefore, we employed a set of complementary spectroscopic techniques to correlate excitons, band structure and material properties for the particular case of WS_2. To image changes in the electronic potential, we used Kelvin probe force microscopy (KPFM). Figure 1c shows a map of variation of the contact potential difference (ΔCPD) of the same monolayer domain as in Figure 1b under ambient conditions. The $\Delta CPD = (\phi_{sample} - \phi_{tip})$ is the difference between the surface potential of the sample (ϕ_{sample}) and the work function of the tip (ϕ_{tip}). The surface potential increases by about $\Delta CDP \approx 100$ meV in the edge region indicating an upwards shift of the bands. We verified this systematic variation of the surface potential for various monolayer domains and for both ambient conditions and dry nitrogen environment (Supporting Information S2). The increase in surface potential is correlated with an increase in PL intensity, as it is clear

by comparing Figure 1b and Figure 1c. In the bright edge region, the PL spectra (Figure 1d) comprise two distinct emission peaks, a main peak X^0 at ~2.0 eV and a low-energy shoulder X^+ at ~1.96 eV. As discussed later in detail, the main peak can be assigned to emission from neutral excitons and the low energy shoulder to emission from trions. By contrast, the spectrum is well described by a single excitonic peak (X^0 at ~1.98 eV) in the dim center region. The slight blue-shift of the exciton from 1.98 eV in the center to 2.0 eV in the edge region would be in agreement with the expected band gap and exciton binding energy renormalization due to an increased density of free charge carriers.[34] We deconvolved each spectrum in the hyperspectral PL maps assuming two Voigt profiles for the contributions X^0 and X^+ (Supporting Information S3). This analysis allows us to plot a histogram of the energy difference between exciton and trion emission E_{X0}-E_{X+} (Figure 1e). Importantly, the histogram demonstrates that the minimum energetic separation is 28 meV, which coincides with the value of the trion binding energy in intrinsic monolayer WS_2.[35] Values E_{X0}-E_{X+} > 28 meV can be understood as the effect of increased free charge carrier density. This finding confirms the tentative assignment of the low energy shoulder in the PL spectrum to the trion. Furthermore, Figs. 1f and 1g demonstrate that the trion emission appears exclusively in the edge region, while the exciton appears throughout the monolayer domain, indicating an increased density of free charge carriers in the edge region. We verified this particular optical structure with distinct center and edge regions for additional monolayer domains (Supporting Information S3). The above histogram analysis provides a simple method to extract the trion binding energy in hyperspectral maps by leveraging intrinsic spatial fluctuations of charge density that modulate the energy separation between trion and exciton emission.

In the following, we will discuss how the observed heterogeneity of the excitonic phenomena is related to the local electronic band structure and ultimately to the material properties. To this end, we employed synchrotron based nano-ARPES equipped with Fresnel zone plate optics for focusing the beam and achieving high spatial resolution (Figure 2a).

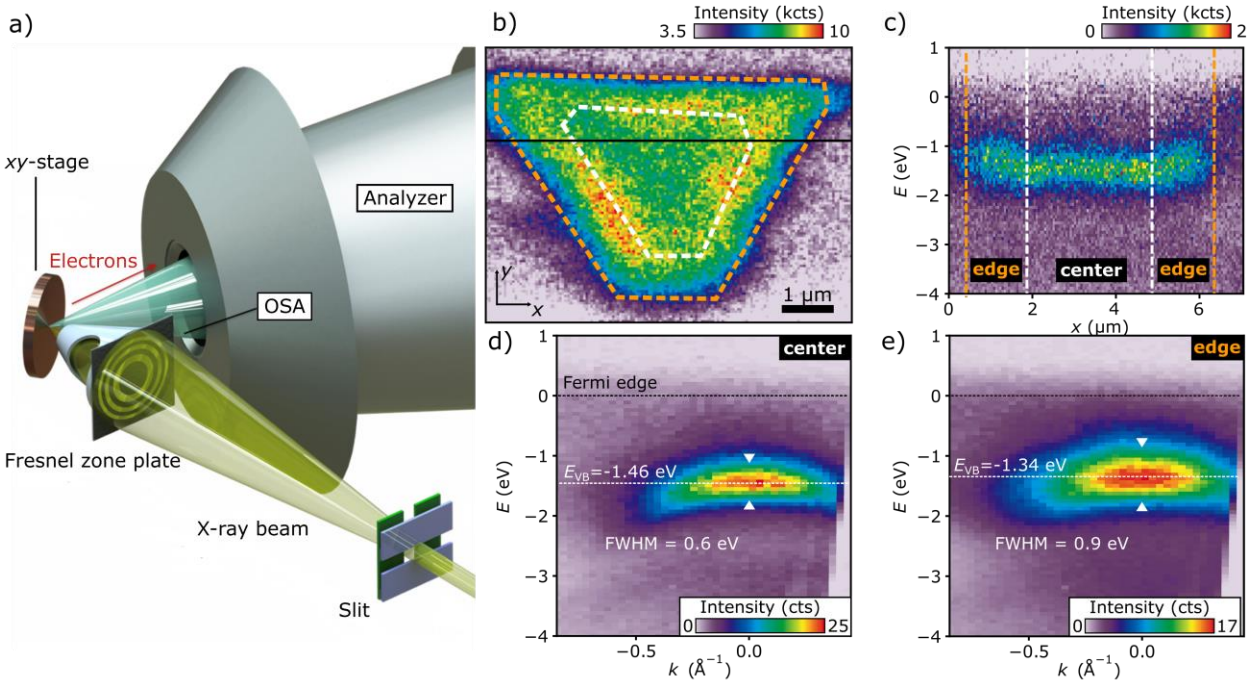

Figure 2. Band structure mapping of monolayer WS_2 by nano-ARPES. **(a)** Schematic of nanoscale photoemission spectroscopy setup of the MAESTRO beamline at the Advanced Light Source. The X-ray beam from the entrance slit (70 µm) is imaged with the help of a Fresnel zone plate and an order sorting aperture (OSA) onto the sample (minimum spot size ~150 nm). Locally emitted photoelectrons are collected by the analyzer, and spatial resolution is achieved by scanning the sample stage. **(b)** Spatial photoemission map integrated around the Γ-point of WS_2. The image resolves a triangular WS_2 monolayer domain on the TiO_2 substrate. **(c)** Line cut $E(x)$ along the black line in **b** revealing distinct edge and center regions. The valence band is shifted upwards in the edge region. The spectrum was integrated in a wide k-range around the Γ-

point bounded by $|k| < 0.4$ Å^{-1}. **(d)** Averaged photoemission spectrum showing the electronic dispersion $E(k)$ from the center of the WS_2 domain (white dashed line in **b**) resolving the valence band near the Γ-point with the band maximum $E_{VB} = -1.46$ eV and FWHM = 0.6 eV (indicated by white triangles). **(e)** Averaged photoemission spectrum $E(k)$ from the edge region (between orange and white dashed lines in **b**). In the edge region, the valence band is significantly broadened (FWHM = 0.9 eV, white triangles) and the spectral valence band maximum is shifted up in energy to $E_{VB} = -1.34$ eV.

Photoemission spectroscopy was carried out at room temperature with an approximately 150 nm wide (FWHM) X-ray spot ($E_{photon} = 98.5$ eV) on the same substrate that was used for the optical characterization, albeit not on the exact same WS_2 domain. However, we verified that the ARPES measurements were taken in a region of the substrate with monolayer domains that showed equivalent morphology and optical properties to the one reported in Figure 1. The full nano-ARPES dataset contains the four-dimensional (E,k,x,y)-dependence of the photoemission intensity, where E is the binding energy, k is the in-plane momentum along a specific direction in the Brillouin zone defined by the detector geometry, and x and y are the spatial coordinates on the sample. It is therefore possible to extract a photoemission spectrum containing the electronic dispersion $E(k)$ at each measured position (x,y) on the sample. To visualize this large dataset, it is instructive to plot integrated spectra that project along specific coordinates. Along this line, Figure 2b shows a spatial photoemission map where the photoemission intensity from the WS_2 valence band was integrated around the Γ-point at $|k| < 0.4$ Å^{-1}. The image resolves a WS_2 domain exhibiting a similar contrast between a center (area within dashed white lines in Figure 2b) and an edge region (area between dashed orange and white lines in Figure 2b) as observed in the PL intensity and surface potential (Figure 1). In Figure 2c, to further visualize how the band

structure changes from the center to the edge region, we plot the energy-resolved photoemission intensity (integrated over the momentum range of $|k| < 0.4$ Å^{-1}) along the horizontal black line in Figure 2b. Figure 2c clearly shows a distinct center and edge region and it is suggestive of an upwards band bending of the valence band at Γ in the edge region. Therefore, Figure 2d and 2e depict the photoemission spectra that are averaged spatially across the center and edge region, respectively. Within the center region, the dispersion of the valence band near the Γ-point is well resolved with a width FWHM = 0.6 eV and maximum at E_{VB} = -1.46 eV. The parameters were extracted from the analysis of the energy and momentum distribution curves around Γ. The Fermi-edge was determined from the continuum of TiO_2 bands and set to E = 0 eV. The values of the linewidth and the valence band maximum at Γ of the as-grown films agree well with a previous study of mechanically transferred films onto identical TiO_2 substrates (FWHM = 550 meV and E_{VB} = 1.43 eV).[22] By contrast, the averaged photoemission spectrum of the edge region (Figure 2e) has a maximum at E_{VB} = -1.34 eV. Furthermore, we find a significant broadening of the overall dispersion to FWHM = 0.9 eV compared to 0.6 eV for the center region. Both the magnitude $\Delta E_{VB} \approx 120$ meV and the spatial pattern of the valence band shift are consistent with the surface potential shift $\Delta CPD \approx 100$ meV measured in KPFM under ambient conditions. We reproduced equivalent results on different monolayer domains (Supporting Information S4). While the CPD can be influenced by the presence of adsorbates at the surface (*e.g.* H_2O or O_2), photoemission experiments were conducted under UHV, thus supporting that the observed potential shift is intrinsic and not caused by surface adsorbates under ambient conditions. The broadening of the valence band rather points towards an increased level of disorder in the edge region due to defects, which in turn may explain the shift of the valence band and the increased free charge carrier density.

To pinpoint the origin of the apparent heterogeneity, we recorded hyperspectral images of the sulfur and tungsten core levels to locally determine the chemical properties of the WS_2 film. In Figs. 3a-3d, we show representative W 4f and S 2p core level spectra that were acquired in the pristine center region (Figs. 3a and 3b) and in the disordered edge region (Figs. 3c and 3d), respectively.

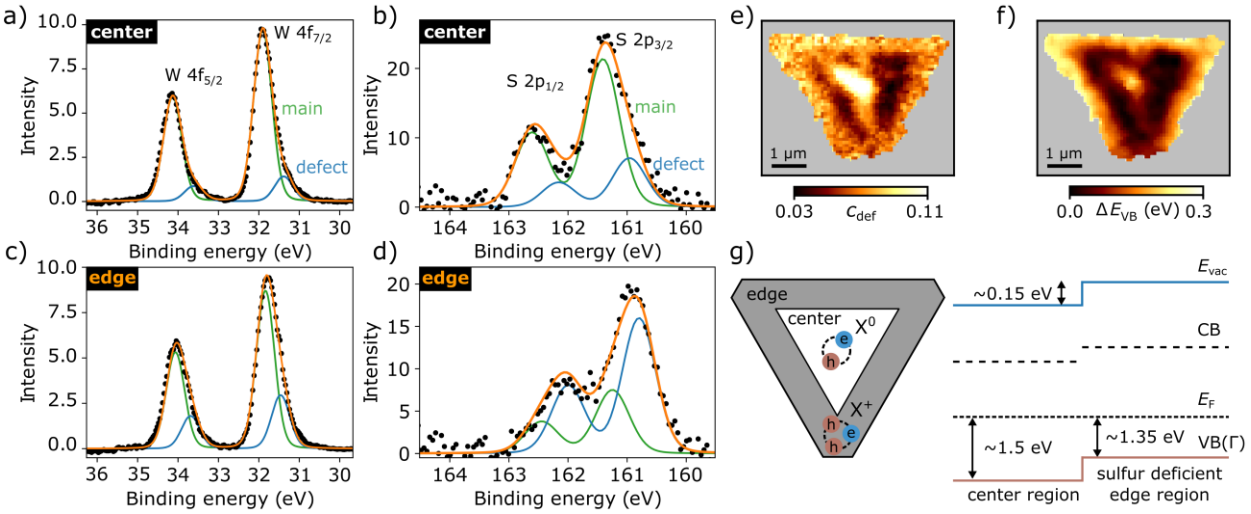

Figure 3. Nanoscale defect imaging by XPS. XPS spectra of the W 4f and S 2p core level measured in the center region **(a,b)** and in the edge region **(c,d)** of a monolayer WS_2 domain. The spectra are deconvolved using a main peak (green), a defect peak (blue) at lower binding energy and their respective spin-orbit doublets. The defect peak arises from sulfur deficient WS_2. **(e)** Spatial map of the defect concentration c_{def} calculated from the areas of the defect and main peak in the W 4f core level spectrum. **(f)** Spatial map of the energetic shift of the valence band maximum ΔE_{VB} extracted from the nano-ARPES data. The shift of the valence band correlates with the concentration of defects in the monolayer WS_2. **(g)** Interplay between defect concentration, band alignment and excitonic properties in monolayer WS_2 domains. Excitonic emission dominates in regions of low defect density. Sulfur deficiency leads to an upwards shift

of the bands by about 0.2 eV and the excitonic emission is modified by trions and/or localized excitons.

The spectra consist of a main spin-orbit doublet at E = 31.8 eV for W 4f and E = 161.4 eV for S 2p matching pristine WS_2 and a second doublet shifted by $\Delta E \approx$ -0.4 eV. The solid lines in Figs. 3a-3d are deconvolved contributions of these doublets for both the sulfur and tungsten spectrum. Details of the XPS analysis are found in S5. Such additional peaks in the core level spectrum of MoS_2 and WS_2 were attributed either to the metallic 1T phase [7,36,37] or sulfur deficiency. [38,39] The presence of a metallic phase is not supported by our ARPES and PL data, and furthermore the observed core level shifts of ΔE_{W4f} = -0.38 eV and ΔE_{S2p} = -0.45 eV are significantly smaller than the reported shift of ΔE = -1 eV for 1T-WS_2.[7] Instead, the core level shift towards smaller binding energies is indicative of reduced WS_{2-x}, *i.e.* sulfur deficiency in the WS_2 film. Accordingly, we label the doublets as main and defect peaks. In the limit of low defect density, the defect density can be estimated by a weighted area ratio of the main and defect peak that takes into account a nearest neighbor interaction on surrounding sulfur and tungsten atoms.[38] Table 1 shows the defect density for the edge and center region estimated from the representative core level spectra in Figure 3a-d.

Table 1. Defect c_{def} concentration from nanoscale XPS.

	center region	**edge region**
c_{def} **from W 4f**	4.2% ± 0.4%	8.7% ± 1.3%
c_{def} **from S 2p**	3.9% ± 0.5%	10.2% ± 0.8%

Importantly, the defect densities calculated from the S 2p spectra are in agreement with those calculated from the W 4f spectra within the experimental error, which further corroborates the assignment of the defect peak to sulfur deficiency.[38] Analysis of the integrated sulfur to tungsten ratio confirms a decrease of the sulfur content by approximately 10% in the edge region compared to the center region (Supporting Information S5). Tungsten oxide core levels would appear at higher binding energies with $\Delta E \approx +3$ eV for WO_3 and $\Delta E \approx +0.3$ eV for WO_2 with respect to WS_2. In the respective energy range we do not detect any significant contributions within the experimental error. Based on the above analysis, we deconvolved the full hyperspectral dataset of the W 4f core level and reconstructed a spatial map of the sulfur deficiency c_{def} (Figure 3e), showing a highly defective edge region ($c_{def} \approx 10\%$) and a moderately defective center region ($c_{def} \approx 3\%$). Furthermore, we also observe an additional highly defective area right at the center of the monolayer domain, which we attribute to nucleation sites of the crystal growth (Figure 1a). This multimodal analysis provides a consistent qualitative picture, but we note that the model in ref. 38 was derived explicitly for low vacancy density, *i.e.* under the assumption of non-neighboring defects. However, in the edge region of the WS_2 domains, the defect density is high and the defect peak becomes comparable to the main peak in the core level spectrum. Therefore, this particular model may fail to accurately estimate the defect density. Furthermore, we cannot exclude contributions from other types of defects, such as anti-site defects, substitutional defects, or defect complexes.[10] In particular, we speculate that also for WS_2 on TiO_2, sulfur vacancies may be efficiently passivated by substitutional atoms as recent results suggest for WS_2 grown on graphene.[41] Finally, we compare the defect density to the variation in valence band position ΔE_{VB} (Figure 3f). The valence band position exhibits a near-perfect correlation with the defect density, and we conclude that the distinct spatial patterns of

PL, surface potential, and valence band share a common origin and can be attributed to domains of abruptly changing defect density within the WS_2 monolayers. Analysis of the S 2p level yields equivalent results (Supporting Information S5). In general, strain originating at intra-grain or layer boundaries can also contribute to excitonic nanoscale heterogeneity in 2D materials.[42] Overall, we find a strong statistical correlation between spatial maps of the intensity of the A_{1g} Raman mode and the energy of the exciton emission, which we interpret as a signature of local strain (Supporting Information S6). However, this appears independent of the apparent distinction between the edge and center region. Consequently, we resolve predominantly the effect of defects on band structure and exciton emission, when comparing edge and center region, superimposed on the smaller effect of local strain. To further corroborate our conclusion of such defect heterogeneity in our samples, we used low temperature photoluminescence spectroscopy. Consistent with the XPS and ARPES analysis, we observe an enhanced emission from defect bound excitons in the edge region at T = 77 K (Supporting Information S7). Our work shows strong agreement with recent experiments that correlated sulfur vacancies at the edges of CVD-grown WS_2 domains, which were resolved by high resolution electron microscopy, to enhanced emission from defect bound excitons.[19] Our results provide further insights how these defects impact the band structure and band alignment expanding the possibility to modify the band structure of 2D materials *via* defect engineering (Figure 3g). Specifically, in the pristine center region, the Fermi level is located approximately mid-gap about 1.5 eV above the valence band at Γ, and the optical properties are dominated by excitons. In the edge region, the increased defect density leads to a broadening and shift of the valence band by about 0.2 eV. Furthermore, the edge region becomes effectively hole doped and the optical properties are dominated by exciton complexes rather than neutral excitons, including positively

charged trions and defect bound excitons. Since the potential shift of the valence band correlates with the work function determined by Kelvin probe microscopy, we can also determine the alignment of the vacuum level as indicated in Figure 3g. We note that the exact conduction band position (indicated by the dotted line in Fig 3g) cannot be inferred directly from the ARPES spectrum or the Kelvin probe spectroscopy. The underlying reason is that the increased charge carrier and defect density in the edge region may lead to a renormalization of the band gap. In principle, measurement of the exciton binding energy by photoluminescence excitation spectroscopy could provide further experimental insights into the interplay of defect density and band renormalization effects.[40]

Conclusions

In summary, we employed spatially resolved photoemission spectroscopy to directly visualize how local modifications of the material chemistry, in particular introduction of sulfur deficiency, change the electronic band structure of synthetic monolayer WS_2. A low temperature chemical vapor deposition process enabled direct synthesis of monolayer WS_2 on conductive TiO_2 substrates for correlated photoemission, Kelvin probe and PL microscopy. With nano-ARPES, we found that high sulfur deficiency introduces a broadening and upwards shift of the valence band by about 300 meV and 120 meV, respectively. This band bending effectively results in the formation of lateral heterointerfaces between intrinsic (pristine) and p-doped (defective) regions. The defective regions occurred exclusively at the edges of the WS_2 crystallites, and they are likely due to variations in the growth process. The spatial distribution of the sulfur defect density exhibits a one-to-one correspondence with emission dominated by trions and defect bound excitons, which we identified by hyperspectral μPL imaging. Thereby, the identified, defect-induced nanoscale band structure modification not only provides a unified picture of nanoscale

heterogeneity, but it also reveals the possibility to precisely tailor lateral heterointerfaces in such two-dimensional materials. The demonstrated capability to map electronic structure and material parameters with high spatial resolution enables precisely exploring extrinsic and intrinsic heterogeneity in 2D materials, such as band bendings in lateral heterostructures or interlayer coupling in vertical heterostructures.

Methods

Synthesis. Monolayer WS_2 was grown by a water-assisted chemical vapor deposition process on Nb-doped rutile (100)-TiO_2 single crystals (*Shinkosha*). The monolayers were synthesized from WO_3 template films that were pre-deposited directly onto the substrate by atomic layer deposition. Perylene-3,4,9,10-tetracarboxylic acid tetrapotassium salt was used as a seeding promoter. The growth took place in a horizontal tube furnace at T = 600 °C under Ar (100 sccm) and H_2S (1 sccm) flow. A detailed description of the process is given in Supporting Information S1.

Optical and morphological characterization of microstructures. Morphology and optical properties of the synthesized structures were characterized by atomic force microscopy (*Park NX-10*, tapping mode) and combined Raman/photoluminescence spectroscopy (*WITEC Alpha 300R*, $\lambda_{excitation}$ = 532 nm, 100x objective, NA = 0.9). The optical power was 100 nW - 1 µW and no photo bleaching was observed. Kelvin probe force microscopy was carried out with a *Bruker Dimension Icon* in frequency modulated peak force mode under ambient conditions and in dry nitrogen atmosphere (rel. humidity < 2%, O_2 < 1%).

Angle resolved photoemission and X-ray photoemission spectroscopy. Angle resolved photoemission intensity maps were recorded using a focused synchrotron beam and a Scienta

R4000 analyzer at the MAESTRO beamline at the Advanced Light Source. A Fresnel zone plate was used as focusing element. For ARPES, the photon energy was set to E_{ph} = 98.5 eV, the detector resolution was 125 meV, and the sample was held at room temperature. For XPS, the photoemission spectra were recorded at a photon energy E_{ph} = 98.8 eV with a detector resolution of 250 meV for W 4f and E_{ph} = 190.7 eV with a detector resolution of 195 meV for S 2p. The base pressure during the measurements was below 10^{-11} mbar. ARPES was conducted on the same substrates as used for KPFM and optical characterization. The samples were grown *ex-situ* (as detailed in Supporting Information S1), exposed to ambient conditions, and then transferred into the nano-ARPES chamber. Prior to the X-ray measurements, the samples were annealed at 200 °C in vacuum for 30 min to remove surface adsorbates.

ASSOCIATED CONTENT

Supporting Information Available: Growth procedure, description of regression analysis, additional nano-ARPES, PL, and KPFM data, statistical analysis of hyperspectral datasets, low temperature PL. This material is available free of charge *via* the Internet at http://pubs.acs.org.

The authors declare no competing financial interest.

AUTHOR INFORMATION

Corresponding Authors

*E-mail: ckastl@lbl.gov

*E-mail: amschwartzberg@lbl.gov

ORCID

Author Contributions

C. K., C. T. C., T. K., S. A., and A. M. S. developed the growth process. J. E. and F. T. contributed Kelvin probe force microscopy. N. J. B. carried out low temperature spectroscopy. R. J. K., S. U., A. B., C. J., and E. R. contributed nanoscale ARPES and XPS. C. K. fabricated the samples, carried out the photoluminescence spectroscopy, and analyzed the data. The manuscript was written through contributions of all authors.

ACKNOWLEDGMENT

Work at the Molecular Foundry and the Advanced Light Source was supported by the Office of Science, Office of Basic Energy Sciences, of the U.S. Department of Energy under Contract No. DE-AC02-05CH11231. J. E. and F. M. T. acknowledge support by the Laboratory Directed Research and Development Program of Lawrence Berkeley National Laboratory under U.S. Department of Energy contract number DE-AC02-05CH11231. S. U. acknowledges funding from VILLUM FONDEN (Grant no. 15375). R. J. K. acknowledges funding from the German Academic Exchange Service (DAAD). A. W.-B., R. J. K., and C. K. were supported by a DOE Early Career Grant.

REFERENCES

(1) Wilson, J. A.; Yoffe, A. D. The Transition Metal Dichalcogenides Discussion and Interpretation of the Observed Optical, Electrical and Structural Properties. *Adv. Phys.* **1969**, *18*, 193–335.

(2) Kuc, A.; Zibouche, N.; Heine, T. Influence of Quantum Confinement on the Electronic Structure of the Transition Metal Sulfide TS_2. *Phys. Rev. B* **2011**, *83*, 245213.

(3) Mak, K. F.; Shan, J. Photonics and Optoelectronics of 2D Semiconductor Transition Metal Dichalcogenides. *Nat. Photonics* **2016**, *10*, 216–226.

(4) Pospischil, A.; Mueller, T. Optoelectronic Devices Based on Atomically Thin Transition Metal Dichalcogenides. *Appl. Sci.* **2016**, *6*, 78.

(5) Voiry, D.; Yang, J.; Chhowalla, M. Recent Strategies for Improving the Catalytic Activity of 2D TMD Nanosheets Toward the Hydrogen Evolution Reaction. *Adv. Mater.* **2016**, *28*, 6197–6206.

(6) Berkelbach, T. C.; Hybertsen, M. S.; Reichman, D. R. Theory of Neutral and Charged Excitons in Monolayer Transition Metal Dichalcogenides. *Phys. Rev. B* **2013**, *88*, 045318.

(7) Voiry, D.; Yamaguchi, H.; Li, J.; Silva, R.; Alves, D. C. B.; Fujita, T.; Chen, M.; Asefa, T.; Shenoy, V. B.; Eda, G.; Chhowalla, M. Enhanced Catalytic Activity in Strained Chemically Exfoliated WS_2 Nanosheets for Hydrogen Evolution. *Nat. Mater.* **2013**, *12*, 850–855.

(8) Tongay, S.; Suh, J.; Ataca, C.; Fan, W.; Luce, A.; Kang, J. S.; Liu, J.; Ko, C.; Raghunathanan, R.; Zhou, J.; Ogletree, F.; Li J.; Grossman, J. C.;& Wu, J. Defects Activated Photoluminescence in Two-Dimensional Semiconductors: Interplay between Bound, Charged, and Free Excitons. *Sci. Rep.* **2013**, *3*, 2657.

(9) Liu, B.; Zhao, W.; Ding, Z.; Verzhbitskiy, I.; Li, L.; Lu, J.; Chen, J.; Eda, G.; Loh, K. P. Engineering Bandgaps of Monolayer MoS_2 and WS_2 on Fluoropolymer Substrates by Electrostatically Tuned Many-Body Effects. *Adv. Mater.* **2016**, *28*, 6457–6464.

(10) Lin, Z.; Carvalho, B. R.; Kahn, E.; Lv, R.; Rao, R.; Terrones, H.; Pimenta, M. A.; Terrones, M. Defect Engineering of Two-Dimensional Transition Metal Dichalcogenides. *2D Mater.* **2016**, *3*, 022002.

(11) Tonndorf, P.; Schmidt, R.; Schneider, R.; Kern, J.; Buscema, M.; Steele, G. A.; Castellanos-Gomez, A.; van der Zant, H. S. J.; de Vasconcellos, S. M.; Bratschitsch, R. Single-Photon Emission from Localized Excitons in an Atomically Thin Semiconductor. *Optica* **2015**, *2*, 347–352.

(12) Klein, J.; Kuc, A.; Nolinder, A.; Altzschner, M.; Wierzbowski, J.; Sigger, F.; Kreupl, F.; Finley, J. J.; Wurstbauer, U.; Holleitner, A. W.; Kaniber, M. Robust Valley Polarization of Helium Ion Modified Atomically Thin MoS_2. *2D Mater.* **2017**, *5*, 011007.

(13) Barja, S.; Wickenburg, S.; Liu, Z.-F.; Zhang, Y.; Ryu, H.; Ugeda, M. M.; Hussain, Z.; Shen, Z.-X.; Mo, S.-K.; Wong, E.; Salmeron, M. B.; Wang, F.; Crommie, M. F.;, Ogletree, D. F.; Neaton, J. B.; Weber-Bargioni, A. Charge Density Wave Order in 1D Mirror Twin Boundaries of Single-Layer $MoSe_2$. *Nat. Phys.* **2016**, *12*, 751–756.

(14) Pulkin, A.; Yazyev, O. V. Spin- and Valley-Polarized Transport across Line Defects in Monolayer MoS_2. *Phys. Rev. B* **2016**, *93*, 041419.

(15) Komsa, H.-P.; Kotakoski, J.; Kurasch, S.; Lehtinen, O.; Kaiser, U.; Krasheninnikov, A. V. Two-Dimensional Transition Metal Dichalcogenides under Electron Irradiation: Defect Production and Doping. *Phys. Rev. Lett.* **2012**, *109*, 035503.

(16) Wang, S.; Lee, G.-D.; Lee, S.; Yoon, E.; Warner, J. H. Detailed Atomic Reconstruction of Extended Line Defects in Monolayer MoS2. *ACS Nano* **2016**, *10*, 5419–5430.

(17) Enyashin, A. N.; Bar-Sadan, M.; Houben, L.; Seifert, G. Line Defects in Molybdenum Disulfide Layers. *J. Phys. Chem. C* **2013**, *117*, 10842–10848.

(18) Liu, X.; Balla, I.; Bergeron, H.; Hersam, M. C. Point Defects and Grain Boundaries in Rotationally Commensurate MoS_2 on Epitaxial Graphene. *J. Phys. Chem. C* **2016**, *120*, 20798–20805.

(19) Carozo, V.; Wang, Y.; Fujisawa, K.; Carvalho, B. R.; McCreary, A.; Feng, S.; Lin, Z.; Zhou, C.; Perea-López, N.; Elías, A. L.; Kabius, B.; Crespi, V. H.; Terrones, M. Optical Identification of Sulfur Vacancies: Bound Excitons at the Edges of Monolayer Tungsten Disulfide. *Sci. Adv.* **2017**, *3*, e1602813.

(20) Bao, W.; Borys, N. J.; Ko, C.; Suh, J.; Fan, W.; Thron, A.; Zhang, Y.; Buyanin, A.; Zhang, J.; Cabrini, S.; Ashby, P. D.; Weber-Bargioni, A.; Tongay, S.; Aloni, S.; Ogletree, D. F.; Wu, J.; Salmeron, M. B.; Schuck, P. J. Visualizing Nanoscale Excitonic Relaxation Properties of Disordered Edges and Grain Boundaries in Monolayer Molybdenum Disulfide. *Nat. Commun.* **2015**, *6*, 7993.

(21) Ogletree, D. F.; Schuck, P. J.; Weber-Bargioni, A. F.; Borys, N. J.; Aloni, S.; Bao, W.; Barja, S.; Lee, J.; Melli, M.; Munechika, K.; Whitelam, S.; Wickenburg, S. Revealing Optical Properties of Reduced-Dimensionality Materials at Relevant Length Scales. *Adv. Mater.* **2015**, *27*, 5693–5719.

(22) Ulstrup, S.; Katoch, J.; Koch, R. J.; Schwarz, D.; Singh, S.; McCreary, K. M.; Yoo, H. K.; Xu, J.; Jonker, B. T.; Kawakami, R. K.; Bostwick, A.; Rotenberg, E.; Jozwiak, C. Spatially Resolved Electronic Properties of Single-Layer WS_2 on Transition Metal Oxides. *ACS Nano* **2016**, *10*, 10058–10067.

(23) Katoch, J.; Ulstrup, S.; Koch, R. J.; Moser, S.; McCreary, K. M.; Singh, S.; Xu, J.; Jonker, B. T.; Kawakami, R. K.; Bostwick, A.; Rotenberg, E.; Jozwiak, C. Giant Spin-Splitting

and Gap Renormalization Driven by Trions in Single-Layer WS_2/h-BN Heterostructures. *Nat. Phys.* **2018,** *14*, 355–359.

(24) Kastl, C.; Chen, C.; Koch, R. J.; Schuler, B.; Kuykendall, T.; Bostwick, A.; Jozwiak, C.; Seyller, T.; Rotenberg, E.; Weber-Bargioni, A.; Aloni, S.; Schwartzberg, A. M. Multimodal Spectromicroscopy of Monolayer WS_2 Enabled by Ultra-Clean van Der Waals Epitaxy. *2D Mater.* **2018,** *5*, 045010.

(25) Latini, S.; Olsen, T.; Thygesen, K. S. Excitons in van Der Waals Heterostructures: The Important Role of Dielectric Screening. *Phys. Rev. B* **2015**, *92*, 245123.

(26) He, J.; Liu, X.; Zhang, W.; Zhao, L.; Liu, D.; He, S.; Mou, D.; Li, F.; Tang, C.; Li, Z.; Wang, L.; Peng, Y; Liu, Y.; Chen, C.; Yu, L.; Liu, G.; Dong, X.; Zhang, J.; Chen, C.; Xu, Z.; *et al.* Electronic Evidence of an Insulator-Superconductor Crossover in Single-Layer FeSe/$SrTiO_3$ Films. *Proc. Natl. Acad. Sci. U. S. A.* **2014**, *111*, 18501–18506.

(27) Eichfeld, S. M.; Hossain, L.; Lin, Y.-C.; Piasecki, A. F.; Kupp, B.; Birdwell, A. G.; Burke, R. A.; Lu, N.; Peng, X.; Li, J.; Azcatl, A.; McDonnell, S.; Wallace, R. M.; Kim, M. J.; Mayer, T. S.; Redwing, J. M.; Robinson, J. A. Highly Scalable, Atomically Thin WSe_2 Grown *via* Metal-Organic Chemical Vapor Deposition. *ACS Nano* **2015**, *9*, 2080–2087.

(28) Li, S.; Wang, S.; Tang, D.-M.; Zhao, W.; Xu, H.; Chu, L.; Bando, Y.; Golberg, D.; Eda, G. Halide-Assisted Atmospheric Pressure Growth of Large WSe_2 and WS_2 Monolayer Crystals. *Appl. Mater. Today* **2015**, *1*, 60–66.

(29) Kastl, C.; Chen, C. T.; Kuykendall, T.; Shevitski, B.; Darlington, T. P.; Borys, N. J.; Krayev, A.; James Schuck, P.; Aloni, S.; Schwartzberg, A. M. The Important Role of Water in Growth of Monolayer Transition Metal Dichalcogenides. *2D Mater.* **2017**, *4*, 021024.

(30) Cain, J. D.; Shi, F.; Wu, J.; Dravid, V. P. Growth Mechanism of Transition Metal Dichalcogenide Monolayers: The Role of Self-Seeding Fullerene Nuclei. *ACS Nano* **2016**, *10*, 5440–5445.

(31) van der Zande, A. M.; Huang, P. Y.; Chenet, D. A.; Berkelbach, T. C.; You, Y.; Lee, G.-H.; Heinz, T. F.; Reichman, D. R.; Muller, D. A.; Hone, J. C. Grains and Grain Boundaries in Highly Crystalline Monolayer Molybdenum Disulphide. *Nat. Mater.* **2013**, *12*, 554–561.

(32) Liu, H.; Lu, J.; Ho, K.; Hu, Z.; Dang, Z.; Carvalho, A.; Tan, H. R.; Tok, E. S.; Sow, C. H. Fluorescence Concentric Triangles: A Case of Chemical Heterogeneity in WS_2 Atomic Monolayer. *Nano Lett.* **2016**, *16*, 5559–5567.

(33) Jeong, H. Y.; Jin, Y.; Yun, S. J.; Zhao, J.; Baik, J.; Keum, D. H.; Lee, H. S.; Lee, Y. H. Heterogeneous Defect Domains in Single-Crystalline Hexagonal WS_2. *Adv. Mater.* **2017**, *29,* 1605043.

(34) Chernikov, A.; van der Zande, A. M.; Hill, H. M.; Rigosi, A. F.; Velauthapillai, A.; Hone, J.; Heinz, T. F. Electrical Tuning of Exciton Binding Energies in Monolayer WS_2. *Phys. Rev. Lett.* **2015**, *115*, 126802.

(35) Plechinger, G.; Nagler, P.; Kraus, J.; Paradiso, N.; Strunk, C.; Schüller, C.; Korn, T. Identification of Excitons, Trions and Biexcitons in Single-Layer WS_2. *Phys. Status Solidi RRL* **2015**, *9*, 457–461.

(36) Eda, G.; Yamaguchi, H.; Voiry, D.; Fujita, T.; Chen, M.; Chhowalla, M. Photoluminescence from Chemically Exfoliated MoS_2. *Nano Lett.* **2011**, *11*, 5111–5116.

(37) He, Q.; Xu, W.; Chen, S.; Liu, D.; Habib, M.; Liu, Q.; Wang, C.; Haleem, Y. A.; Xiang, T.; Wu, C.; Khalil, A.; Fang, Q; Niub Z.; Song, L. *In Situ* Growth of Metallic 1T-WS_2 Nanoislands on Single-Walled Carbon Nanotube Films for Improved Electrochemical Performance. *RSC Adv.* **2016**, *6*, 87919–87925.

(38) Donarelli, M.; Bisti, F.; Perrozzi, F.; Ottaviano, L. Tunable Sulfur Desorption in Exfoliated MoS_2 by Means of Thermal Annealing in Ultra-High Vacuum. *Chem. Phys. Lett.* **2013**, *588*, 198–202.

(39) Shpak, A. P.; Korduban, A. M.; Kulikov, L. M.; Kryshchuk, T. V.; Konig, N. B.; Kandyba, V. O. XPS Studies of the Surface of Nanocrystalline Tungsten Disulfide. *J. Electron Spectrosc. Relat. Phenom.* **2010**, *181*, 234–238.

(40) Yao, K.; Yan, A.; Kahn, S.; Suslu, A.; Liang, Y.; Barnard, E. S.; Tongay, S.; Zettl, A.; Borys, N. J.; Schuck, P. J. Optically Discriminating Carrier-Induced Quasiparticle Band Gap and Exciton Energy Renormalization in Monolayer MoS_2. *Phys. Rev. Lett.* **2017**, *119*, 087401.

(41) Barja, S.; Refaely-Abramson, S.; Schuler, B.; Qiu, D. Y.; Pulkin, A.; Wickenburg, S.; Ryu, H.; Ugeda, M. M.; Kastl, C.; Chen, C.; Hwang, C.; Schwartzberg, A.; Aloni, S.; Mo, S.-K.; Ogletree, D. F.; Crommie, M. F.; Yazyev, O. V.; Louie, S. G.; Neaton, J. B.; Weber-Bargioni, A. Identifying Substitutional Oxygen as a Prolific Point Defect in Monolayer Transition Metal Dichalcogenides with Experiment and Theory. *arXiv*:1810.03364.

(42) Zheng, Y.; Chen, J.; Ng, M.-F.; Xu, H.; Liu, J. P.; Li, A.; O'Shea, S. .J.; Dumitrică, T.; Loh, K. P. Quantum Mechanical Rippling of a MoS_2 Monolayer Controlled by Interlayer Bilayer Coupling. *Phys. Rev. Lett.* **2015,** *114,* 065501.

For Table of Contents Only